Hindawi
Geofluids
Volume 2022, Article ID 8704344, 13 pages
https://doi.org/10.1155/2022/8704344

Research Article

A Method for the Inversion of Reservoir Effective Permeability Based on Time-Lapse Resistivity Logging Data and Its Application

Hairong Zhang,[1] **Bin Zhao**,[1] **Shiqi Dong**,[2] **Xixin Wang**,[3] **and Pengfei Jing**[2]

[1]*College of Geophysics and Oil Resources, Yangtze University, Wuhan Hubei, China*
[2]*Southern Marine Science and Engineering Guangdong Laboratory (Zhanjiang), Zhanjiang, China*
[3]*College of Geosciences, Yangtze University, Wuhan Hubei, China*

Correspondence should be addressed to Bin Zhao; zhaobin@yangtzeu.edu.cn

Received 20 January 2022; Revised 8 March 2022; Accepted 31 March 2022; Published 22 April 2022

Academic Editor: Kouqi Liu

Effective permeability is a key parameter for evaluating reservoirs and their productivity. With the wide application of resistivity logging tools in drilling, the advantages of resistivity logging in response to the dynamic invasion process of drilling fluids have become increasingly prominent. We analyzed the variation law of the measured resistivity data for different permeability formations at different times. In this study, we proposed an effective permeability modeling method based on the time-lapse resistivity logging data. First, based on the resistivity measurement data at different times, the dynamic resistivity profile of the reservoir was obtained through joint inversion; we then obtained the invasion depth and invasion zone resistivity of the drilling fluid at different times, along with the original formation resistivity. Subsequently, combined with parameters such as the soaking time, fluid viscosity, and saturation change of the drilling fluid, we obtained the phase permeability curve of the reservoir and dynamic effective permeability of the fluid near the wellbore. This study provides basic parameters for subsequent formation analyses and productivity prediction and substantially improves the reservoir evaluation technology from static to dynamic.

1. Introduction

The seepage characteristics of the reservoir are key parameters that control the decision-making for its completion, oilfield development, and reservoir management. The most important parameter for evaluating the seepage characteristics of a reservoir is the effective permeability and can be obtained through testing. However, the cost of testing is extremely high; therefore, the effective permeability is generally extrapolated by the absolute permeability of the laboratory, such as core analysis, log comparison, and well testing [1–6]. The existing methods for obtaining effective permeability have certain limitations in practical applications. For example, core analysis provides an average permeability equivalent to a few cubic inches of samples, and the sample size is too small to describe a reservoir in general terms. However, the scale of formation testing is several thousand cubic feet and cannot provide a detailed description of the reservoir heterogeneity. In view of the aforementioned limitations, an increasing number of scholars at home and abroad have begun to characterize the microscopic pore structure and seepage characteristics of reservoirs through numerical simulation techniques through digital cores, especially in the field of unconventional reservoirs such as shale oil and shale gas [7–13]. With the development of logging and drilling technology, many scholars have begun to pay attention to the multi-angle correlation between the logging data and reservoir permeability. In the early stages, foreign scholars proposed a method of inversion to obtain the absolute permeability of the reservoir by combining the measured data from three types of tools, such as resistivity logging, neutron logging, and density logging, through the

history matching method [14–17]. To ensure the reliability of the formation permeability parameters obtained through resistivity logging and other data, scholars began to use nuclear magnetic resonance (NMR), formation testing, pump sampling, and other data to correct the inversion results and estimate the relative permeability curve and capillary pressure of the reservoir curve [18–21]. Through a comparative study, we observed that the main aim of previous research was to invert the permeability of the reservoir by comparing the measured and simulated curves; however, less attention has been paid to the dynamic resistivity profile of the reservoir after considering the drilling fluid invasion and reservoir rocks. The quantitative relationship between the physical parameters, especially the dynamic change in the resistivity profile of the reservoir, is caused by the difference in logging time and reservoir permeability.

The Dongfang Block in western South China Sea is a high-pressure gas field. The well sections of the target layers were all measured using the Schlumberger ARC675 electromagnetic wave resistivity logging tool (ARC675); the resistivity logging is commonly affected by the drilling fluid. Considering the phenomenon of low invasion effect, repeated logging was conducted in each well logging operation, and there was abundant time-lapse resistivity logging data. Considering the actual measurement of electromagnetic wave resistivity while drilling in this area, the author combined the vector finite element method and front-line solution method to solve the forward model of the logging-while-drilling (LWD) resistivity response. The dynamic resistivity profiles of the formation, including the drilling fluid invasion depth, invasion zone resistivity at different times, and the undisturbed formation resistivity, were combined with the changes in formation drilling time, fluid viscosity, and saturation to obtain discrete phase permeability curve characteristic points. The functional relationship between saturation and relative permeability was obtained by fitting the least squares algorithm. Finally, the dynamic effective permeability of the fluid near the wellbore was obtained according to the saturation curve at different times.

2. Method of Joint Inversion of Time-Shift Resistivity

The combined inversion results based on the resistivity logging data at different times can accurately reflect the changing process of the dynamic invasion of the reservoir drilling fluid. First, the vector finite element method was used according to the Maxwell equation of electromagnetic wave response. This method began from the formation model (including the layered structure of the wellbore) to simulate the measurement response of electromagnetic wave resistivity while drilling in the nonuniform formation and to establish and verify a forward modeling method. On this basis, three sets of formation models were constructed as the solution parameters, namely, the radius of the invasion zone (Ri), the resistivity of the invasion zone (Rxo), and the formation resistivity (Rt). The drilling fluid invasion depth, resistivity of the invasion zone, and true resistivity of the formation were obtained at different times, and the dynamic resistivity profile was obtained to provide basic data for the subsequent calculation of the effective permeability.

2.1. Method of Joint Inversion of Time-Shift Resistivity. Measurement theory of electromagnetic wave resistivity while drilling involves solving Maxwell's equations under the given boundary conditions [22]. The electromagnetic field in the logging problem satisfies the following Maxwell equation:

$$\nabla \times E = -\mathrm{i}\omega\mu H \tag{1}$$

$$\nabla \times H = \sigma E + J \tag{2}$$

According to Equations (1) and (2), we deduced that the vector wave equation satisfied by the electric field is

$$\nabla \times \nabla \times E - \omega^2 \mu \varepsilon_c E = -\mathrm{j}\omega\mu J \tag{3}$$

where $\varepsilon_c = \varepsilon - i\sigma/\omega$ is the complex dielectric constant and ε is the dielectric constant of the formation.

In layered structured media, the numerical simulation of electrical logging tools is vital for obtaining the tool parameters in complex environments. Several numerical methods have been successfully applied to simulate complex media, including the finite difference time domain (FDTD), finite element method (FEM), and numerical mode matching (NMM). The author first established a physical model of the layered stratigraphic structure including the wellbore (as shown in Figure 1), discretized the stratigraphic model space according to the electromagnetic field distribution law, and then established a two-dimensional discrete grid space (as shown in Figure 2). The vector finite element method and the front-line solution method were combined to solve the aforementioned Maxwell equation to realize the forward modeling of the measurement response of the electromagnetic wave resistivity while drilling in the nonuniform formation. To verify the reliability of the forward modeling model and algorithm, the Schlumberger's ARC675 instrument was used as an example to conduct relevant forward modeling simulations, and the results were verified with the Schlumberger calibration plate for accuracy.

Figures 3(a), 3(b), 4(a), and 4(b) show the comparison results of the borehole calibration chart for the ARC675 tool. In the chart, the abscissa is the apparent resistivity (Rps and Rad are the apparent resistivities of the phase difference and amplitude ratio, respectively), and the ordinate is the true value of the formation and apparent resistivity. The ratio between resistivity represents the correction factor. Compared with the Schlumberger borehole calibration chart, the data error of each source distance chart was less than 3%, indicating that the forward modeling algorithm was reliable.

2.2. Time-Shift Resistivity Joint Inversion. Joint inversion refers to the inversion of geological model parameters using two or more types of logging data with different physical mechanisms [23]. The resistivity data collected at different

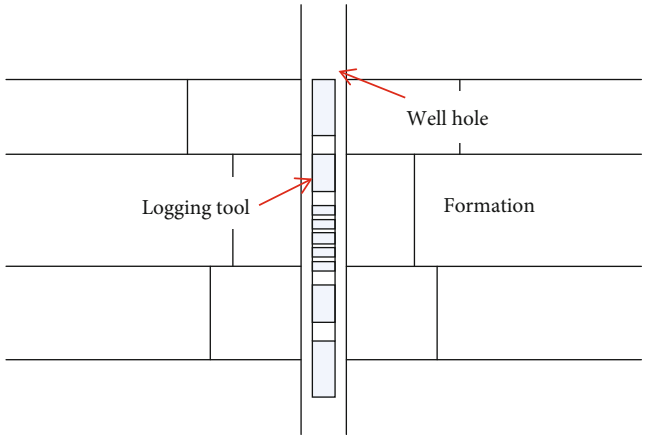

Figure 1: Physical model of the vertical well.

times have different invasion depths and resistivity values of the invasion zone due to the different soaking times of the drilling fluid. However, the resistivity of the undisturbed formation is unique, and the time-lapse resistivity joint inversion can more accurately reflect the geological model parameters because it increases the amount of effective information for the specific detection targets. Compared with the static resistivity profile of iterative inversion, the dynamic resistivity profile of the reservoir was obtained by inversion by considering the influence of logging time on the resistivity profile.

The time-lapse resistivity joint inversion is based on the damped least-squares method and organically unifies the resistivity logging response at different times and the dynamic profile of the formation resistivity for inversion. First, the least-squares objective function is constructed, assuming that y is the actual measured logging curve data and $f(x)$ is the response function of the tool to the formation model, and the objective function is assumed to be in the form of the sum of squares:

$$\varphi\left(\vec{x}\right) = \sum_{k=1}^{m}\left[y_k - f_k\left(\vec{x}\right)\right]^2 \tag{4}$$

where m is the number of logging curves and f is the multivariate nonlinear response function for the parameters. The response function is related to the working principle of the tool, structure of the tool, and formation model. This is the parameter to be inverted, including the resistivity measurement at time T1. A total of five sets of formation model parameters can be obtained through the foregoing resistivity forward model to solve for $f(x)$: namely, the intrusion zone radius *Ril*, intrusion zone resistivity *Rxol* at time T2, intrusion zone radius *Rih*, intrusion zone resistivity *Rxoh* when the resistivity is measured at T2, and the formation resistivity *Rt*.

Marquette's algorithm was used to solve the least-squares problem. Gauss proposed a linearization method to expand $f(\vec{x})$ into a Taylor series near $\vec{x}^{(0)}$ and omit the quadratic term $\vec{\delta}_i$ and the above quadratic terms. The formula used is as follows:

$$f_k\left(\vec{x}^{(0)} + \vec{\delta}\right) = f_k\left(\vec{x}^{(0)}\right) + \sum_{i=1}^{n}\frac{\partial\left(\vec{x}\right)}{\partial x_i}\Big|_{\vec{x}=\vec{x}^{(0)}}\vec{\delta}_i \tag{5}$$

It is abbreviated as

$$f\left(\vec{x}^{(0)} + \vec{\delta}\right) = f\left(\vec{x}^{(0)}\right) + p\vec{\delta} \tag{6}$$

where p is called the Jacobian matrix.

$$p_{m\times n} = \begin{pmatrix} \frac{\partial f_1}{\partial x_1} & \cdots & \frac{\partial f_1}{\partial x_n} \\ \vdots & \ddots & \vdots \\ \frac{\partial f_m}{\partial x_1} & \cdots & \frac{\partial f_m}{\partial x_n} \end{pmatrix} \tag{7}$$

The linear approximate expression of the function after substituting Equation (6) into Equation (4) is as follows:

$$\begin{aligned}\varphi\left(\vec{x}^{(0)} + \vec{\delta}\right) &= \left[\vec{y} - \vec{f}\left(\vec{x}^{(0)}\right) - p\vec{\delta}\right]^T\left[\vec{y} - \vec{f}\left(\vec{x}^{(0)}\right) - p\vec{\delta}\right] \\ &= \left[\vec{y} - \vec{f}\left(\vec{x}^{(0)}\right)\right]^T\left[\vec{y} - \vec{f}\left(\vec{x}^{(0)}\right)\right] \\ &\quad - 2\left[\vec{y} - \vec{f}\left(\vec{x}^{(0)}\right)\right]p\vec{\delta} + \vec{\delta}^T p^T p\vec{\delta}\end{aligned} \tag{8}$$

The purpose of this equation is to solve the minima of the function φ; thus, $\vec{\delta}$ should satisfy the following conditions:

$$\frac{\partial\varphi}{\partial\vec{\delta}} = -2P^T\left[\vec{y} - \vec{f}\left(\vec{x}^{(0)}\right)\right] + 2P^T P\vec{\delta} = 0 \tag{9}$$

wherein,

$$A\vec{\delta} = \vec{g} \tag{10}$$

in the formula:

$$A = P^T P \tag{11}$$

$$\vec{g} = P^T\left[\vec{y} - \vec{f}\left(\vec{x}^{(0)}\right)\right] \tag{12}$$

Therefore,

$$\vec{\delta} = A^{-1}\vec{g} \tag{13}$$

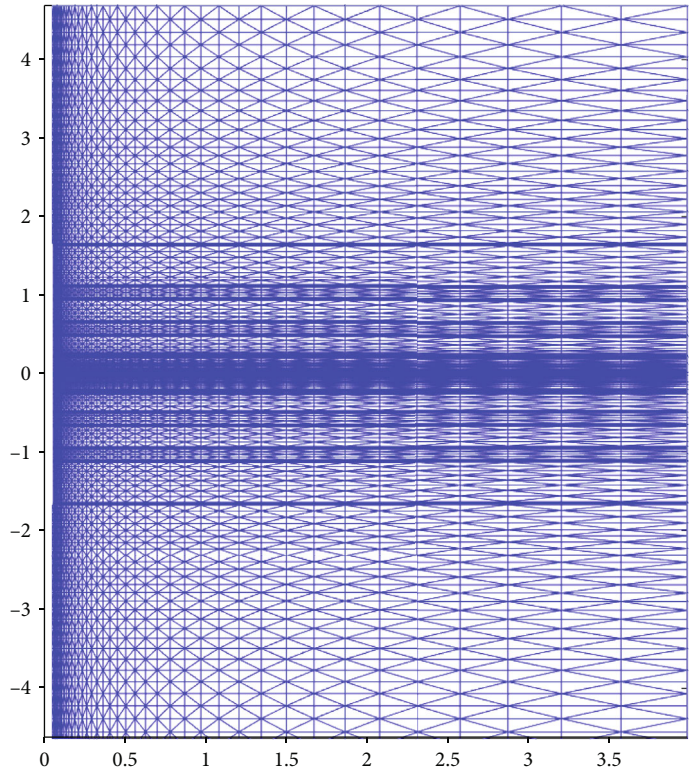

Figure 2: 2D grid of the stratigraphic model.

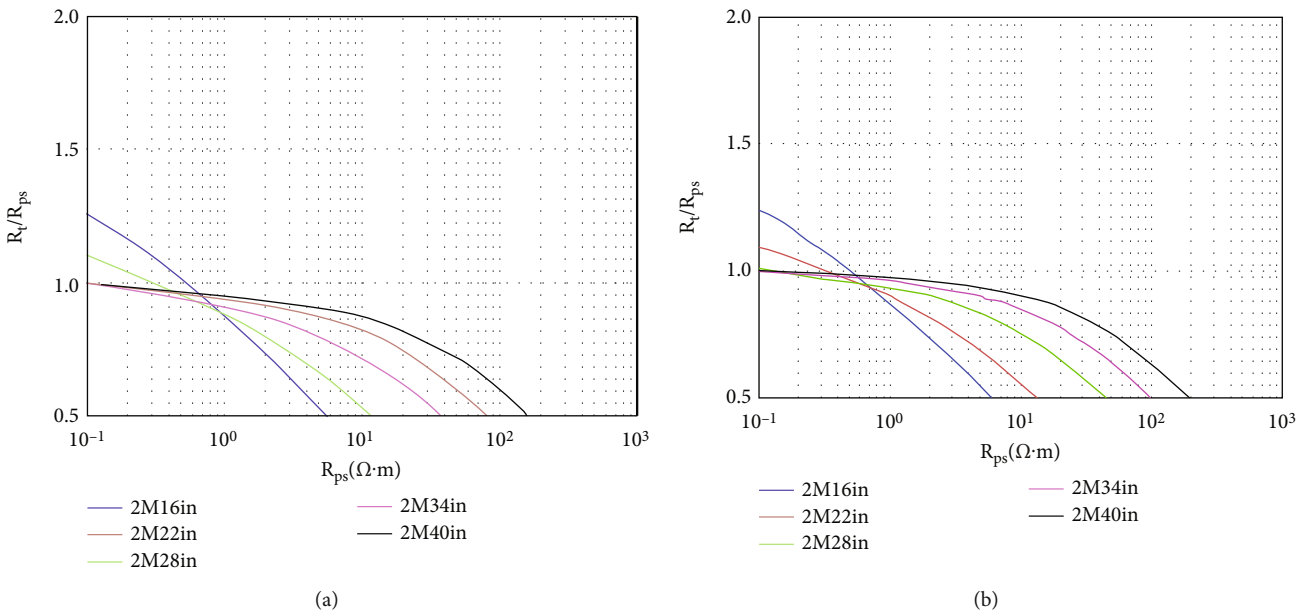

Figure 3: (a) Charts of ARC675 (2 MHz, dh = 14 in, Rm = 0.02 Ω · m) in the references. (b) Charts of ARC675 (2 MHz, dh = 14 in, Rm = 0.02 Ω · m) in this paper.

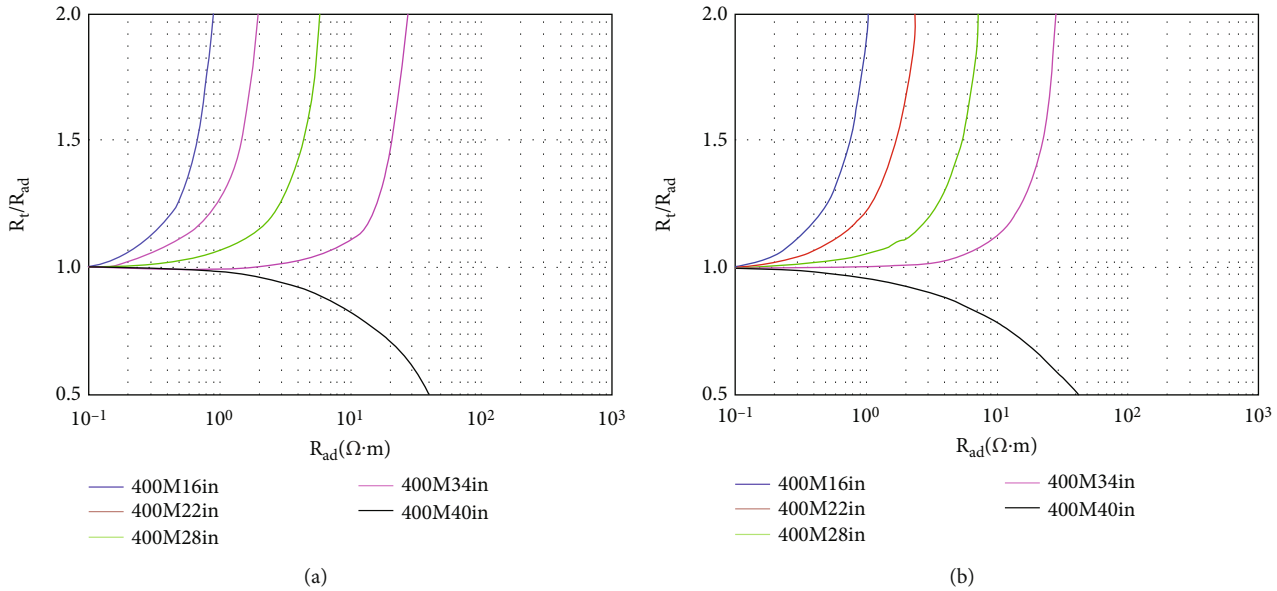

Figure 4: (a) Charts of ARC675 (400 kHz, dh = 14 in, Rm = 0.02 Ω · m) in the references. (b) Charts of ARC675 (400 kHz, dh = 14 in, Rm = 0.02 Ω · m) in this paper.

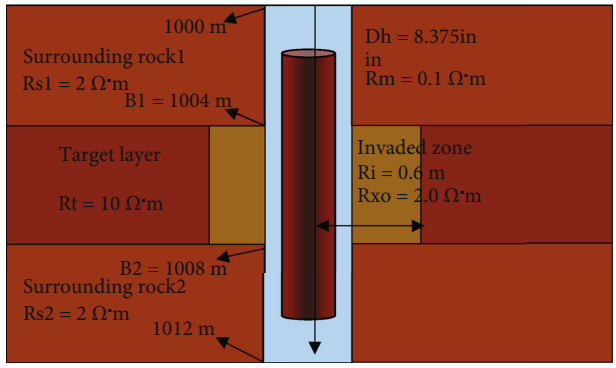

Figure 5: Schematic diagram of the time-lapse resistivity joint inversion formation model.

To prevent the appearance of the local optimal solution and improve the convergence of the solution, we introduced a damping factor η, and Equation (13) is transformed into

$$\vec{\delta} = (A + \eta I)^{-1}\vec{g} \tag{14}$$

where I is the identity matrix.

In practical problems, when the observed value is given, the appropriate model and initial values are selected; P, A, $\vec{g}$, and $\vec{\delta}^{(0)}$ can be obtained.

$$\vec{x}^{(1)} = \vec{x}^{(0)} + \vec{\delta}^{(0)} \tag{15}$$

Subsequently, $\vec{x}^{(1)}$ is considered the initial value, and the calculation is repeated to find $\vec{\delta}^{(1)}$ until the absolute value $\sum|\vec{\delta}^{(k)}|$ of component of $\vec{\delta}^{(k)}$ is less than the error ε given in advance.

2.3. Joint Inversion Convergence and Confidence. A three-layer stratigraphic model (Figure 5) was used to examine the convergence and confidence of the joint inversion. The stratigraphic model is rotationally symmetric about the well axis and is uniform. The model parameters are set as follows: The formation thickness is 4.0 m, the formation interface values are 1004.0 and 1008.0 m, the borehole diameter is $Dh = 8.375$ in, the mud resistivity is $Rm = 0.1\,\Omega\cdot$m, the upper and lower surrounding rock formation resistivity values are $Rs1 = Rs2 = 2.0\ \Omega\cdot$m, the radius of the invasion zone while drilling in the target layer is Ri = 0.6 m, the resistivity of the invasion zone while drilling is $Rxo = 2.0\,\Omega\cdot$m, and the formation resistivity is $Rt = 10.0\,\Omega\cdot$m. The sampling point range and sampling interval are 1000.0 to 1012.0 m and 0.2 m, respectively; a total of 61 points were used.

The resistivity joint inversion of the model was conducted according to the above model parameter settings, and the results are shown in Figure 6. The first trace in the figure is the invasion depth trace, and the blue dotted line is the inversion result of the model invasion radius. The third trace is the resistivity trace, and the red dotted line is the model formation true resistivity inversion result. The green dotted line in the *RXOL* curve is the model inversion of intrusive zone resistivity. The remaining curves show the phase difference and attenuation resistivity results obtained by inversion.

We analyzed the errors of the invasion radius, invasion zone resistivity, and true formation resistivity obtained by model inversion. As presented in Table 1, the relative errors of the three parameters were within 1.5%, and the inversion

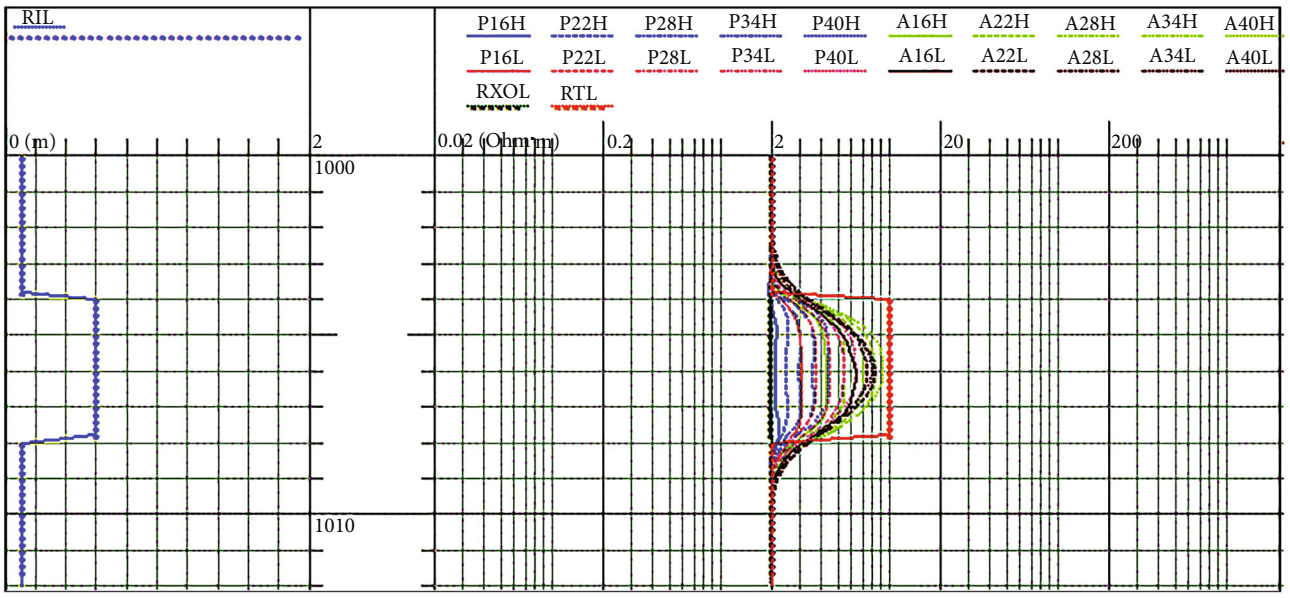

Figure 6: Inversion results.

Table 1: Evaluation of the inversion results.

Parameter	True value	Inversion initial value	Inversion results	Error
RT (Ω•m)	10	13	9.92	0.83%
Rxo (Ω•m)	2	2.5	1.97	1.31%
RiL (m)	0.6	0.48	0.59	0.85%

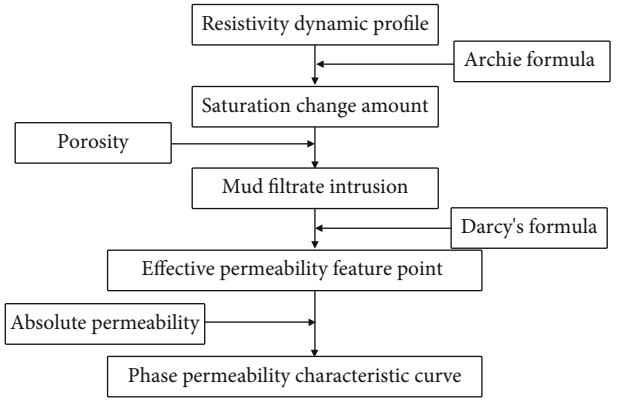

Figure 7: Flow chart of the construction of the phase permeability characteristic curve.

exhibited good convergence. This result converges to the true value.

3. Construction Method of the Characteristic Permeability Curve

The time-lapse resistivity joint inversion considers the logging time factor; therefore, the inversion obtains the dynamic resistivity profile of the reservoir. The change in the dynamic profile of the reservoir was mainly caused by the invasion of mud filtrate into the formation to replace the movable oil and gas in it with the passage of logging time. The change in the formation resistivity reflects the change in the formation fluid saturation, and the change in saturation reflects the intrusion of the mud filtrate. The intrusion amount of mud filtrate per unit time is related to the permeability of each phase fluid; therefore, the effective permeability of the reservoir can be obtained by further analysis based on the dynamic resistivity profile of the joint inversion.

Figure 7 shows the basic flow chart of the effective permeability construction. First, based on the dynamic resistivity profile of the reservoir, the resistivity is converted into saturation parameters using Archie's formula, including the water saturation in the invasion zone and that in the original formation. The saturation change amount ΔS_{wx} of the intrusion zone at the intrusion depth is as follows:

$$\Delta S_{wx} = \sqrt[n]{\frac{a * R_{\mathrm{mf}}}{\varnothing^m * R_{xo}}} - \sqrt[n]{\frac{a * R_{\mathrm{w}}}{\varnothing^m * R_t}}, \tag{16}$$

Assuming that the porosity of the reservoir remains unchanged during mud invasion, the change in volume of the fluid water in the rock can be obtained by combining the definitions of porosity and saturation (Equation (19)). Combined with the specific logging time (i.e., the drilling fluid soaking time), the flow formula (Equation (20)) can be calculated, namely, the invasion amount of the mud filtrate per unit time (q):

$$S_w = \frac{V_w}{V_p}, \tag{17}$$

$$\varnothing = \frac{V_P}{V_b}, \tag{18}$$

$$V_w = \Delta S_{wx} * \varnothing * V_b, \tag{19}$$

$$\mathrm{q} = \frac{\Delta Sw_x * \varnothing * \pi * R_i^2 * H}{\Delta \mathrm{T}}, \tag{20}$$

where $\varnothing$ is the formation porosity, V_b is the rock volume of the reservoir, ΔT is the logging interval, ΔSw_x_x is the change in water saturation, R_i is the drilling fluid invasion depth at the ΔT interval, and H is the reservoir thickness.

By combining the initial pressure of the formation and the pressure difference of the drilling string, the permeability of the water phase can be deduced by substituting Equation (20) into Darcy's formula (21). As we considered the real logging environment when calculating the saturation change, namely, the simultaneous existence of multiphase fluids (water, oil, or gas) in the rock, the calculated permeability at this time is the effective permeability of the water phase.

$$\mathrm{q} = \frac{\mathrm{K} * \Delta P \bullet \mathrm{A_c}}{\mu \bullet \Delta L}, \tag{21}$$

$$K_{ew} = \frac{\Delta Sw_x * \varnothing * \pi * R_i^2 * H * \mu_w * R_i}{2\pi * R_h * \mathrm{H} * (P_m - P_w) * \Delta \mathrm{T}} = \frac{\Delta Sw_x * \varnothing * R_i^3 * \mu_w}{2 * R_h * (P_m - P_w) * \Delta \mathrm{T}}, \tag{22}$$

where K_{ew} is the effective permeability of the water phase, R_h denotes the wellbore radius, μ_w denotes the viscosity of water, P_m denotes the pressure of the drilling string, and P_w denotes the initial pressure of the undisturbed formation.

Assuming that there are only two-phase fluids in the reservoir, and that they are incompatible and incompressible, because the total reservoir fluid saturation remains unchanged, the amount of change in water saturation in the invasion zone and that in oil and gas saturation remains the same. In a complementary relationship, the intrusion of mud filtrate in the reservoir is equal to the displacement of oil and gas, and the effective permeability of oil and gas can be obtained similarly. The relative permeability of each fluid phase can be obtained by calculating the ratio of the effective permeability to the absolute permeability.

$$K_{\mathrm{rw}} = \frac{K_{\mathrm{ew}}}{K}, \tag{23}$$

$$K_{\mathrm{rnw}} = \frac{K_{\mathrm{enw}}}{K}, \tag{24}$$

The effective permeability calculated above was constructed based on the dynamic resistivity profile of the reservoir, and the dynamic resistivity profile of the reservoir was obtained based on the time-lapse resistivity curve using the joint inversion technique. Therefore, the constructed phase-permeability curve is a discrete characteristic phase permeability curve. It is necessary to obtain a continuous functional relationship between saturation and relative permeability using data fitting technology. The basic functional relationship between saturation and relative permeability is modified by the Brooks-Corey model as follows:

$$\mathrm{K}_{rw} = \mathrm{K}_{rw0} * (\mathrm{S_{we}})^{ew}, \tag{25}$$

$$\mathrm{K}_{rnw} = \mathrm{K}_{rnw0} * (1 - \mathrm{S_{we}})^{enw}, \tag{26}$$

Among them, K_{rw0}, K_{rnw0}, *ew*, and *enw* represent the undetermined coefficients to be solved; K_{rw0} and K_{rnw0} represent the relative permeability endpoint values of the aqueous and non-aqueous phases; *ew* and *enw* represent the exponential coefficients; and $\mathrm{S_{we}}$ represents the effective saturation, which is defined as:

$$S_{\mathrm{we}} = \frac{S_w - S_{wi}}{1 - S_{wi} - S_{gr}}, \tag{27}$$

where S_{wi} is the irreducible water saturation and S_{gr} is the residual oil and gas saturation.

4. Oilfield Application Examples

Well xx adopted a drill bit diameter of 8.375 in; the drilling fluid type was PDF-THERM; the mud resistivity was 0.23 at 23.89 ˚C; the mud filtrate resistivity is 0.09 at 27.2 ˚C; and the reservoir lithology was gray mudstone and siltstone. Schlumberger's EcoScope was the electromagnetic wave resistivity instrument used while drilling, including two time-lapse resistivity measurement datasets of real-time measurement during the drilling and upward remeasurement. The reservoir porosity was 14-19%, and the permeability was 5-62 mD. The resistivity curves of different probing depths measured in real time during drilling were separated to some extent, indicating that a certain amount of drilling fluid invaded the formation. Compared with those measured in real time, the resistivity curves of different probing depths remeasured, while drilling exhibited a greater decrease in resistivity. This shows that the drilling fluid invaded deeper and the change in resistivity corresponded well with the permeability of the reservoir, as shown in Figure 8.

4.1. Reservoir Dynamic Resistivity Profile Inversion. Figure 9 shows the combined inversion results of the main and remeasured resistivity logging in a well, including the invasion depth and invasion zone resistivity measured in real time during drilling, invasion depth and invasion zone resistivity of remeasurement while drilling, and true resistivity of the formation. The first trace in the figure represents the invasion depth trace, including the gamma curve and the inversion depth of the mud invasion at different times. *LXO_T1_INV* represents the mud invasion depth of joint inversion measured in real time, and *LXO_T2_INV* represents the remeasured mud invasion depth of the joint inversion. The third and fourth traces show a comparison of the phase difference and amplitude-specific resistivity curves measured in real time, along with the joint inversion results of the resistivity of the invasion zone and true resistivity of the formation, respectively. Traces 5 and 6 show the

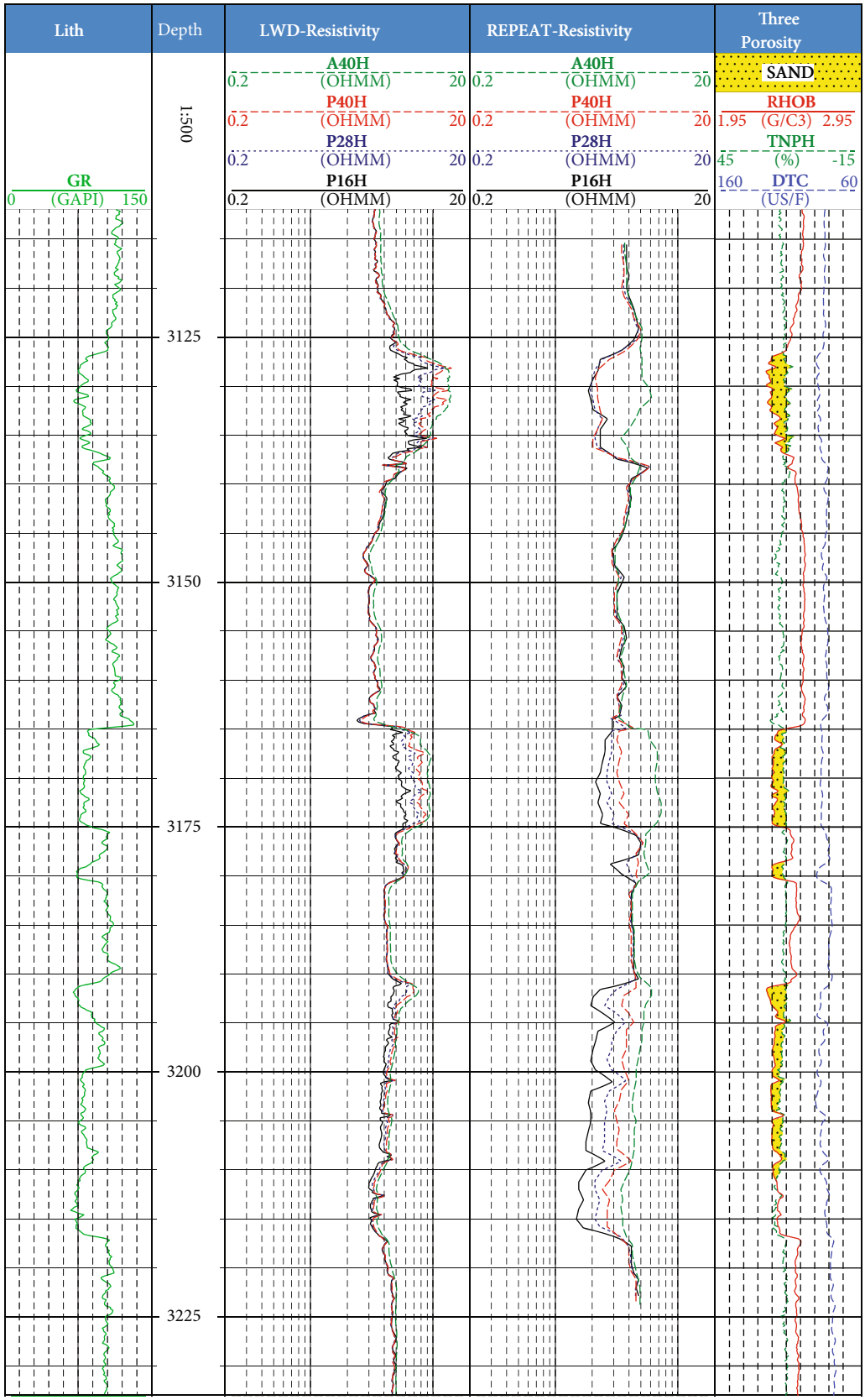

Figure 8: Electromagnetic wave resistivity measurement curve of well xx during the drilling and re-measurement.

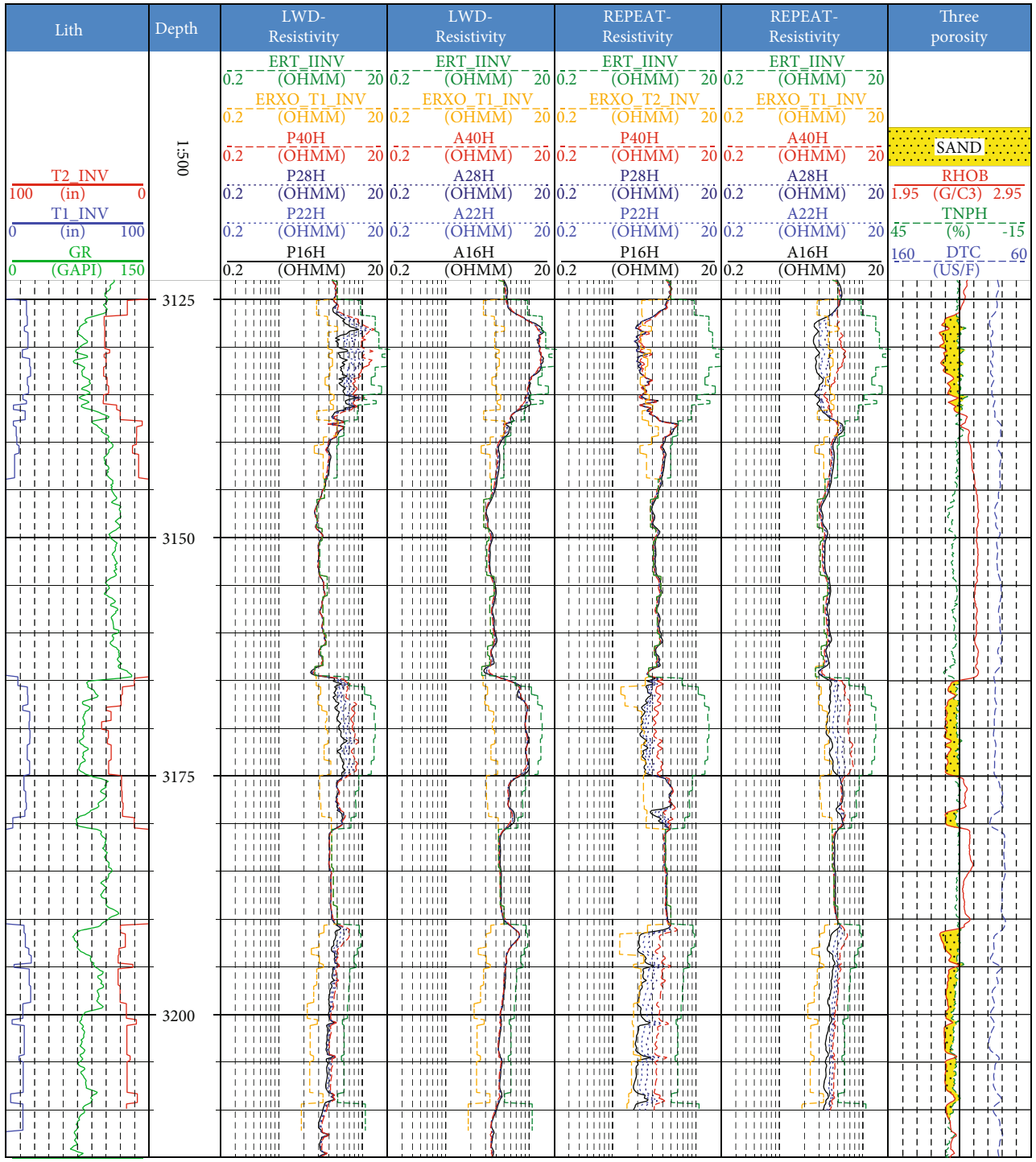

Figure 9: Results of joint inversion of electromagnetic wave resistivity while drilling in well xx at different times.

comparison of the phase difference and amplitude-specific resistivity curves obtained by the remeasurement using the combined inversion results of the resistivity of the invasion zone and true resistivity of the formation, respectively. *ERXO_T1_INV* represents the intrusion zone resistivity of joint inversion measured in real time, *ERXO_T2_INV* represents the remeasured intrusion zone resistivity of the joint inversion, and *ERT_IINV* represents the true resistivity of joint inversion. The seventh trace represents the neutron density porosity curve. The above joint inversion results showed that the inversion depth curve has a good corresponding relationship with the *GR* lithology curve, as well as with the neutron density curve. The remeasured mud filtrate of the combined inversion of the reservoir with large porosity and good permeability has a greater invasion depth, which demonstrates the rationality of the inversion results.

Table 2: Physical parameters and joint inversion results of the target interval.

Layer number	Top depth m	Bottom depth m	Porosity %	Permeability mD	LXO_T1 In	LXO_T2 In	Rxo_T1 Ω.m	Rxo_T2 Ω.m	Rt Ω.m
1	3126.8	3133.0	16.79	19.02	14.87	30.79	4.1	2.4	17.10
2	3133.0	3137.0	14.62	4.99	13.04	28.13	4.0	2.5	12.76
4	3165.1	3166.4	15.44	8.25	12.43	15.48	3.0	1.7	9.28
5	3166.7	3175.2	16.33	14.63	15.56	26.98	3.6	2.2	13.45
6	3178.6	3180.6	16.28	20.39	7.45	12.49	3.9	2.7	7.55
7	3191.0	3192.6	17.23	37.11	13.23	17.61	3.2	1.6	9.48
8	3192.6	3194.5	16.69	20.00	16.03	20.21	2.8	1.7	8.63
10	3195.1	3200.6	16.76	20.39	14.87	19.04	2.6	2.0	6.84
12	3201.2	3204.0	18.74	61.73	12.76	15.51	2.4	1.8	6.06
14	3204.8	3208.1	18.10	41.60	11.88	15.25	2.4	1.7	6.03

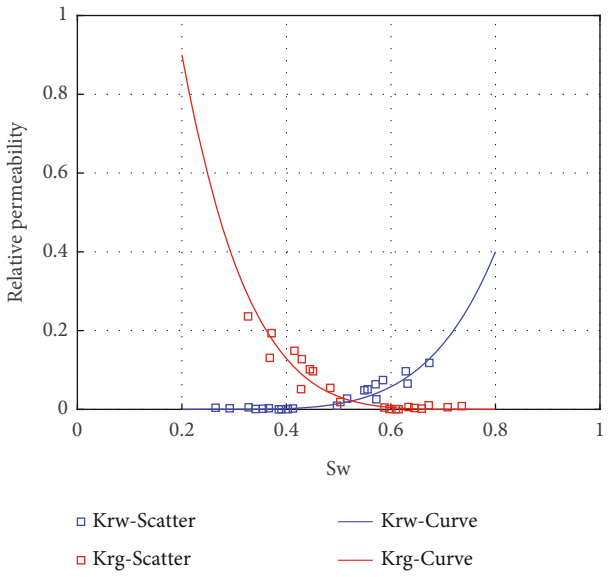

Figure 10: Characteristic scattered permeability curve diagram.

4.2. Determination of Permeability Characteristic Scattering Points and Construction of Permeability Curve. The dynamic resistivity profile of the reservoir is based on the "layer-to-layer" joint inversion, which expresses the variation law of the electrical profile of the reservoir after drilling-fluid invasion at different times. Therefore, the obtained permeability is the characteristic point of the effective permeability in the near-wellbore zone after drilling fluid invasion at a certain time. Assuming that the porosity of the reservoir remains unchanged during the process of mud filtrate invasion, the pressure difference between the pressure of the drilling fluid column and that of the original formation is experienced on both sides of the formation invasion zone, and the resistivity and saturation are converted using Archie's equation. The cementation index and porosity index adopt regional empirical values such as $m = 1.6$ and $n = 1.8$; the coefficient $a = 0.23$; the formation water resistivity (Rw), mud filtrate resistivity (Rmf), and viscosity of formation water are 0.21 Ω.m, 0.09 Ω.m, and 1.01×10^{-6} m^2/s, respectively; and the gas viscosity under formation conditions is 2.75×10^{-6} m^2/s. Table 2 lists the average values of the resistivity, invasion depth, porosity, permeability, and other curves of each target feature layer.

Combined with the above reservoir physical parameters and joint inversion results, Equations (16), (22), (23), and (24) can be used to obtain the characteristic phase dispersion point of the target interval; and a characteristic scatter point phase permeability curve relationship diagram is obtained (Figure 10). Based on the data shown in Figure 10, the functional relationship between the water saturation and the relative permeability of each fluid phase can be obtained by fitting Equations (28) and (29).

The fitting function relationship between the formation water saturation and relative permeability of water is

$$K_{rw} = 0.4 * (S_{we})^{4.8}. \tag{28}$$

The fitting function relationship between the formation water saturation and relative permeability of gas is

$$K_{rg} = 0.9 * (1 - S_{we})^{4.8}, \tag{29}$$

where S_{we} represents the effective saturation, which is defined as

$$S_{we} = \frac{S_w - S_{wi}}{1 - S_{wi} - S_{gr}}, \tag{30}$$

where S_{wi} represents the irreducible water saturation and S_{gr} represents the residual gas saturation. During actual data processing, the S_{wi} and S_{gr} values need to be selected in combination with the core analysis results. We conducted a comprehensive analysis of the core NMR and high-temperature and high-pressure gas-water permeability experimental results of the actual application case wells to obtain the irreducible water saturation of the treated well section; S_{gr} and S_{wi} are both 0.2.

4.3. Effective Penetration Rate and Its Damage Analysis. Based on the aforementioned relationship curve of

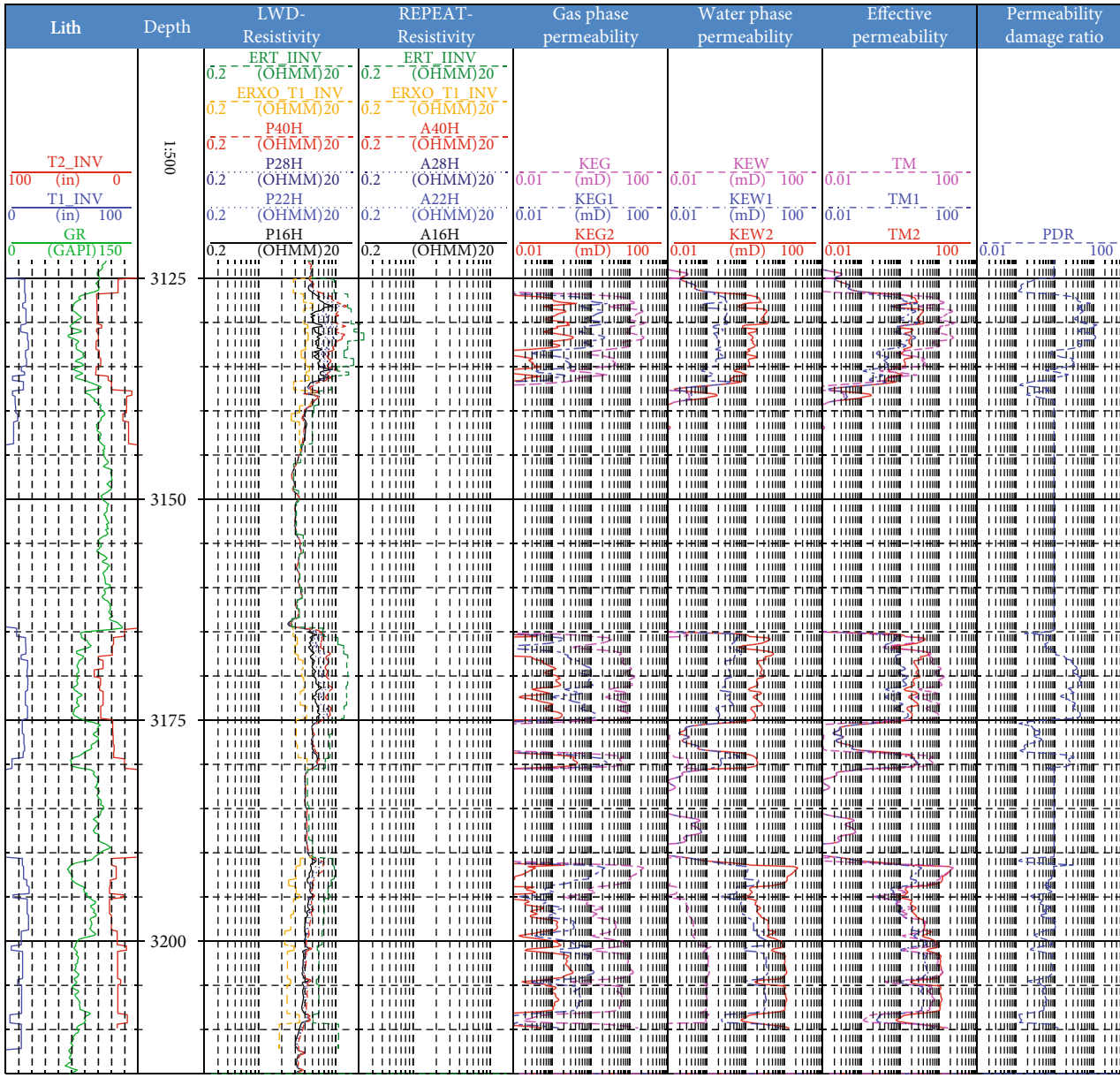

Figure 11: Effective permeability and permeability damage results of well xx.

saturation and relative permeability, combined with the dynamic resistivity profile of the reservoir inversion and the logging permeability, a continuous effective permeability curve can be obtained; this includes the original formation (before drilling fluid invasion) and the effective permeability of the gas and water phases at time 1 of real-time logging (drilling fluid immersion for 1 h) and time 2 of re-logging (drilling fluid immersion for 3 h). KEG and KEW in Figure 11 represent the effective permeability curves of the gas and water phases of the undisturbed formation, respectively; *KEG1* and *KEW1* represent the effective permeability curves of the gas and water phases at time 1 of real-time logging; *KEG2* and *KEW2* represent the effective permeability curves of the gas and water phases at time 2 of re-logging; *TM*, *TM1*, and *TM2* represent the comprehensive fluid effective permeability curve of the original formation, real-time logging time 1, and re-logging time 2, respectively, namely, the fluid flow capacity. *PDR* represents the permeability damage ratio of the reservoir, which is defined both in the original formation and during the re-logging measurement; comprehensive permeability ratio and *PDR* values less than 1 in a well at time 2 indicate that the reservoir has been benignly improved; a *PDR* value equal to 1 indicates that the reservoir is free of pollution; and *PDR* values greater than 1 and larger indicate a strong pollution degree of the reservoir. The third trace is the electromagnetic wave resistivity curve during drilling and the joint inversion result at time 1 of real-time logging; the fourth trace is the electromagnetic wave resistivity curve during drilling and the joint inversion result at time 2 of re-logging; the fifth trace shows the effective permeability of the gas phase at different times in the near-wellbore zone; the sixth trace represents the

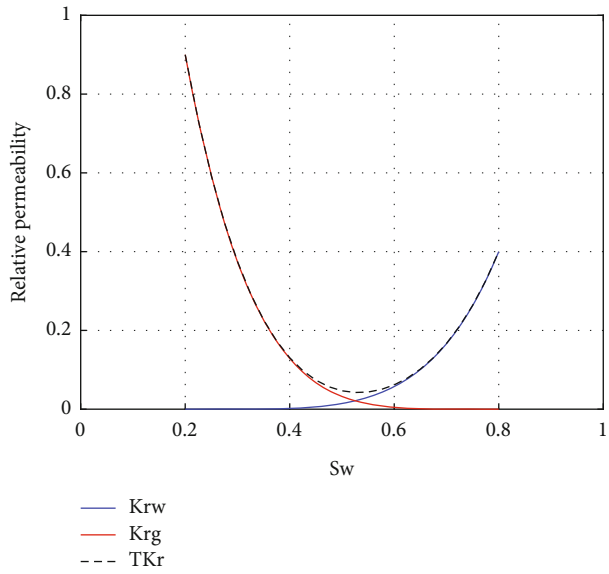

Figure 12: Permeability curve of each phase fluid and comprehensive phase permeability curve.

water phase effective permeability in the near-wellbore zone at different times; the seventh trace represents the comprehensive fluid mobility capacity of the near-wellbore zone at different times; and the eighth trace represents the coefficient of the reservoir PDR.

From the above calculation results, we observed that the gas layer sections (3126-3137 m and 3165-3175 m) are affected by the drilling fluid invasion; only the effective permeability of the gas phase of the well zone gradually decreases and that of the water phase gradually increases. The effective permeability of the water phase near the wellbore was almost zero before drilling fluid invasion, indicating that the saturated water in the formation was irreducible. In the gas-water interval (3200-3208 m) affected by the drilling fluid invasion, the variable law of the effective permeability of the gas and water phases in the near-wellbore zone is consistent with that of the pure gas interval; however, the variation amplitude is smaller than that of the pure gas interval. The effective permeability of the gas and water phases in the near-wellbore zone before the drilling fluid invasion in the same interval of gas and water is not zero, indicating that it contains both movable water and gas. The permeability and PDR curve shows that the 3126-3137 m interval of the gas reservoir is seriously polluted, the 3165-3175 m interval is slightly polluted, and the 3200-3208 m interval of the gas-water reservoir is slightly improved. From the comprehensive permeability curve of the reservoir fluid, the effective permeability of the reservoir before and after drilling fluid invasion in the pure gas interval decreases, while that of the reservoir in the same gas and water interval increases. In particular, as the water saturation of the reservoir increases, the variation law of the integrated fluid in the reservoir shows that the permeability decreases first and increases subsequently (TKr curve in Figure 12).

5. Conclusions

(1) The time-lapse resistivity logging data and reservoir dynamic and static permeability have multi-angle correlations. The characteristic phase permeability curve calculation model can be derived using Darcy's formula, the resistivity dynamic invasion profile, and the water saturation model. By combining the regional interpretation model, we realized an effective permeability evaluation of reservoirs based on time-lapse resistivity logging. The calculation results are more representative than the effective permeability parameters obtained by conventional core analysis and more accurately reflect the seepage characteristics of the reservoir

(2) By comprehensively analyzing the dynamic resistivity profile of the reservoir, and combined with the calculated effective permeability parameters of the reservoir before and after drilling fluid invasion, we obtained the permeability damage ratio of the reservoir. This ratio can provide guidance for evaluating reservoir pollution and testing the formation

(3) This study did not consider the differences in the relative permeability curves of different reservoirs when calculating the effective permeability. To improve the accuracy of the effective permeability calculation results, it is necessary to analyze the variation law of the characteristic relative permeability curves of the reservoirs in the study area and select the appropriate relative permeability according to the reservoir-type and curve parameters

Data Availability

The well data used to support the findings of this study are available from the corresponding author upon request.

Conflicts of Interest

The authors declare that they have no conflicts of interest.

References

[1] D. Yang, H. R. Zhang, Y. X. Wu, H. R. Zhang, and W. Tan, "Application of cable formation test data in productivity prediction of low permeability gas reservoirs," *China Offshore Oil and Gas*, vol. 30, no. 6, pp. 109–114, 2019.

[2] P. C. Dong, Z. W. Ma, and C. S. Zhao, "Evaluating method of relative permeabilities of a reservoir," *Petroleum Geology & oilfield Development in Daqing*, vol. 27, no. 6, pp. 55–58, 2008.

[3] L. Jaedong and M. John, "Enhance wireline formation tests in low-permeability formations quality control through formation rate analysis," *Rocky Mountain Regional/Low-Permeability Reservoirs Symposium and Exhibition*, 2000.

[4] H. Liu, W. H. Wang, M. G. Chen, Q. G. Liu, and X. H. Hu, "Seepage experiment and mathematical model of multi-scale shale reservoir," *Journal of Xi'an Shiyou University (Natural Science Edition)*, vol. 33, no. 4, pp. 66–71, 2018.

[5] S. S. Gao, W. Xiong, and X. G. Liu, "Experimental research status and several novel understandings on gas percolation mechanism in low permeability sandstone gas reservoirs," *Natural Gas Industry*, vol. 30, no. 1, pp. 52–55, 2010.

[6] H. Lei, Y. H. Zheng, J. H. He, and Z. G. Hu, "A new method for physical simulation of flow characteristics of fluids in shale oil reservoirs," *Acta Petrolei Sinica*, vol. 42, no. 10, pp. 1346–1356, 2021.

[7] F. R. Wang, S. He, and Y. H. Zheng, "Mineral composition and brittleness characteristics of the inter-salt shale oil reservoirs in the Qianjiang Formation," *Petroleum Geology & Experiment*, vol. 38, no. 2, pp. 211–218, 2016.

[8] C. N. Zou, Z. Yang, and J. W. Cui, "Formation mechanism geological characteristics and development strategy of non-marine shale oil in China," *Petroleum Exploration and Development*, vol. 40, no. 1, pp. 15–27, 2013.

[9] Y. L. Su, H. Wang, S. Y. Zhan, W. D. Wang, and J. L. Xu, "Research progress on characterization and simulation of shale oil flow in microscale," *Journal of Shenzhen University (Science and Engineering)*, vol. 38, no. 6, pp. 579–589, 2021.

[10] L. C. Kuang, L. H. Hou, and Z. Yang, "Key parameters and methods of lacustrine shale oil reservoir characterization," *Acta Petrolia Sinica*, vol. 41, no. 1, 2021.

[11] F. Javadpour, H. Singh, A. Rabbani, M. Babaei, and S. Enayati, "Gas flow models of shale: a review," *Energy & Fuels*, vol. 35, no. 4, pp. 2999–3010, 2021.

[12] T. Zhang, X. F. Li, Y. Yin et al., "The transport behaviors of oil in nanopores and nanoporous media of shale," *Fuel*, vol. 242, no. 12, pp. 305–315, 2019.

[13] A. Oblger, J. Ulmf, and R. Pellenq, "Impact of nano-porosity on hydrocarbon transporting shales' organic matter," *Nano Letters*, vol. 18, no. 2, pp. 832–837, 2018.

[14] D. P. Tobola and S. A. Holditch, "Determination of reservoir permeability from repeated induction logging," *SPE Formation Evaluation*, vol. 6, no. 1, pp. 20–26, 1991.

[15] C. Y. Yao and S. A. Holditch, "Reservoir permeability estimation from time-lapse log data," *SPE25513*, 1993.

[16] M. Jesús, "Estimation of permeability from borehole array induction measurements: application to the petrophysical appraisal of tight gas sands," *PETROPHYSICS*, vol. 47, no. 6, pp. 527–544, 2006.

[17] M. Jesús, "Automatic estimation of permeability from array induction measurements: applications to field data," in *SPWLA 46th Annual Logging Symposium*, New Orleans, Louisiana, USA, 2005.

[18] S. J. Li and L. C. Shen, "Dynamic invasion profiles and time-lapse electrical logs," in *SPWLA 44th Annual Logging Symposium*, Galveston, Texas, USA, 2003.

[19] L. Lin and S. H. Wang, "Estimating in-situ relative permeability and capillary pressure from multiphysics wireline measurements," in *SPWLA 59th Annual Logging Symposium*, Old Billingsgate, London, UK, 2018.

[20] N. David and S. J. Li, "Invasion effects on time-lapsed array induction logs," in *SPWLA 48th Annual Logging Symposium*, Austin, Texas, USA, 2007.

[21] J. S. Chen and A. Dicman, "Physics-based permeability modeling," in *SPWLA 52th Annual Logging Symposium*, Colorado Springs, Colorado, 2011.

[22] D. G. Wu, J. Chen, and C. R. Liu, "An efficient FDTD method for axially symmetric LWD environments," *IEEE*, vol. 46, no. 6, pp. 1652–1656, 2008.

[23] S. Alireza, T. Michael, and A. Lori, "Carbonate formation evaluation using joint inversion of resistivity and dielectric logs," in *SPWLA 58th Annual Logging Symposium*, Oklahoma City, Oklahoma, USA, 2017.